ARTICLE IN PRESS

Journal of Fluids and Structures xxx (xxxx) xxx

Contents lists available at ScienceDirect

Journal of Fluids and Structures

journal homepage: www.elsevier.com/locate/jfs

Vortex-induced vibration of elastically-mounted spheres: A comparison of the response of three degrees of freedom and one degree of freedom systems

Methma M. Rajamuni *, Mark C. Thompson, Kerry Hourigan

Fluids Laboratory for Aeronautical and Industrial Research (FLAIR), Department of Mechanical and Aerospace Engineering, Monash University, Clayton, Victoria 3800, Australia

ARTICLE INFO

Article history:
Received 1 November 2018
Received in revised form 31 January 2019
Accepted 4 February 2019
Available online xxxx

Keywords:
3-DOF motion
Vortex-induced vibration
Circular trajectory
Spiralling wake

ABSTRACT

In published literature of the vortex-induced vibration of a sphere, limited attention has been devoted to spheres having three degrees of freedom (DOF) motion and the effect on the vibration response. In this study, the vortex-induced vibration response of a 3-DOF elastically-mounted sphere was examined numerically. The response of a sphere allowed to oscillate in all three spatial directions (3-DOF motion) was compared with the response of a sphere whose motion was restricted to only the transverse direction (1-DOF). Simulations were conducted over the reduced velocity range $U^* \equiv U/(Df_n) \in [3.5, 16]$, using a sphere of mass ratio $m^* \equiv \rho_s/\rho = 3$, at a fixed Reynolds number of 2000, where U is the free-stream velocity of the flow, f_n is the natural frequency of the system, ρ_s and ρ are the solid and fluid densities, respectively. When the sphere was allowed 3-DOF movement, it was initially excited to vibrate along a linear path in the transverse direction, synchronized with the two-sided shedding of vortex loops behind the sphere. As the simulation time advanced, the sphere trajectory eventually converted into a circular orbit with a spiralling wake behind it. The transition time between these two modes was found to increase with decreasing Reynolds number. The vibration amplitude was significantly smaller when the sphere motion was in all three spatial directions than when it was restricted only to the transverse direction. The maximum vibration amplitudes were approximately 0.6 and 0.8 diameters, for 3-DOF and 1-DOF motion, respectively. In the synchronization regime, the maximum time-averaged drag coefficient was approximately 100% greater than that of a stationary sphere, when the sphere had 3-DOF, similar to previous observations for a tethered sphere. However, the maximum change to the time-averaged drag coefficient was only 76% when the motion was restricted to the transverse direction.

1. Introduction

A significant volume of research has been focused on vortex-induced vibration (VIV) over the past decades, owing to its practical significance to many engineering fields. VIV of a bluff body is a periodic vibration state induced by vortex shedding from the body leading to an oscillatory force on it. In particular, for a sphere, periodic or quasi-periodic vortex loops form behind the body, exciting it to vibrate when the vortex shedding frequency is close to the natural frequency of the system. As

* Corresponding author.
E-mail addresses: methma.rajamuni@monash.edu, methma.mm@gmail.com (M.M. Rajamuni).

https://doi.org/10.1016/j.jfluidstructs.2019.02.005
0889-9746/

Please cite this article as: M.M. Rajamuni, M.C. Thompson and K. Hourigan, Vortex-induced vibration of elastically-mounted spheres: A comparison of the response of three degrees of freedom and one degree of freedom systems. Journal of Fluids and Structures (2019), https://doi.org/10.1016/j.jfluidstructs.2019.02.005.

this robust vibration state can be sustained for a long time, it can cause fatigue damage or even catastrophic failure. Therefore, it is important to understand the nature of VIV at a deep level. Due to the complexity and non-linearity of vibration problems, it is not possible to treat them analytically. Therefore, the fundamentals of vortex-induced vibration, and the more general case of flow-induced vibration, have been disclosed through extensive experimental and computational studies examining the response of generic bluff bodies. Major findings can be found in comprehensive reviews by Bearman (1984), Parkinson (1989), Sarpkaya (2004), Williamson and Govardhan (2004, 2008), Wu et al. (2012) and Ern et al. (2012).

Due to their geometric simplicity and symmetries, cylinders and spheres are the most studied geometries that have been used to investigate the fundamentals of flow-induced vibration. In particular, a vast amount of research has been undertaken with freely vibrating circular (or square) cylinders, due to their practical importance and simplicity of setting up such arrangements both experimentally and computationally. In contrast, only a relatively small amount of research has been conducted on freely vibrating spherical bodies. Thus, the wake of an axisymmetric body, like a sphere, is less well understood, and there are some important questions yet to be fully addressed.

A freely vibrating sphere was first examined in depth by Govardhan and Williamson (1997) and Williamson and Govardhan (1997). They conducted experiments with tethered spheres that revealed that the sphere also vibrates vigorously, like a cylinder, when placed in a uniform flow field. The sphere vibrated with a maximum amplitude as large as the diameter of the sphere. The transverse oscillation frequency was half that of the streamwise oscillation frequency, despite the fact that the natural frequency of a tethered body is independent of direction. This led the sphere to follow a path in the shape of a 'figure eight', with a streamwise amplitude of 0.2 diameters. The streamwise amplitude was found to decrease with increasing mass ratio, resulting in the typical sphere trajectory changing from a 'figure eight' to a 'crescent' shape (Govardhan and Williamson, 1997; Williamson and Govardhan, 1997; Govardhan and Williamson, 2005; Jauvtis et al., 2001).

Based on the amplitude response curve (A^* – U^*), Govardhan and Williamson (1997) identified two different sphere responses in the reduced velocity range $U^* \approx [0, 20]$, which are known as modes I and II. Here, $U^* \equiv U/(Df_n)$ and $A^* \equiv \sqrt{2}A_{rms}/D$ are the non-dimensional velocity of the flow known as reduced velocity and non-dimensional amplitude of the sphere vibration, respectively, where U is the upstream flow velocity, D is the diameter of the sphere, f_n is the natural frequency of the system, and A_{rms} is the r.m.s. of the sphere vibration amplitude. The experimental studies of Jauvtis et al. (2001) and Govardhan and Williamson (2005) investigated these two modes further by varying the mass ratio, $m^* \equiv \rho_s/\rho$, over a wide range, where ρ_s and ρ are the solid and fluid densities, respectively. The sphere showed a mode I response over a small range of reduced velocities ($U^* \approx [5, 6]$) before it gradually transitioned to a mode II response with increasing U^*. Both of these modes are vortex-induced vibration responses, where the sphere vibrates in synchrony with the vortex shedding frequency and the natural frequency of the system. The mode I response can be identified as the natural resonance, which is more robust than the mode II response (Rajamuni et al., 2018b). Interestingly, the vibration amplitude of mode II was found to be larger than the amplitude of mode I (nearly double) at high Reynolds numbers. Govardhan and Williamson (1997) observed a local peak in the amplitude response curve for mode I with light spheres ($m^* < 1$). However, this peak was obscured for heavy spheres ($m^* > 1$), especially when mounted with elastic supports, leading to a smooth amplitude response curve. Govardhan and Williamson (2005) reported that when the mass ratio and mass-damping parameter, $m^*\zeta$, was systematically increased, then the synchronization regime narrowed, while the response amplitude decreased, ζ is the damping ratio. Govardhan and Williamson (2005) visualized the wake behind the sphere using PIV measurements and found two trails of hairpin vortex loops for both mode I and II states.

The experimental studies of van Hout et al. (2010, 2013) over the Reynolds number ranges $Re \equiv DU/\nu \in [486, 5556]$ and $Re \in [493, 2218]$, respectively, and the computational study of Pregnalato (2003) at $Re = 500$, also reported highly periodic VIV responses with tethered spheres in the mode I and II regimes, ν is the kinematics viscosity of the fluid. The combined experimental and computational study of Lee et al. (2013) investigated the vibration response of a neutrally buoyant ($m^* = 1$) sphere, over a wide range of Reynolds numbers, ranging from 50 to 12 000, and identified seven distinct flow regimes. They found that the sphere started to vibrate as a result of the onset of vortex shedding for $Re \gtrsim 270$. Based on the sphere trajectories, they identified three distinct periodic vibration regimes over the Reynolds number range $270 \leq Re \leq 550$. Moreover, the sphere showed an irregular motion for $Re \in [550, 3000]$ and quasi-circular motion for $Re > 3000$.

Mi and Gottlieb (2015) derived a Lagrangian-based model to estimate both structural and aeroelastic parameters, for light spheres ($m^* < 1$). Validation of the model was demonstrated by comparison of results with those of Govardhan and Williamson (1997) and Constantinescu and Squires (2000). They revealed the existence of possible quasi-periodic and non-stationary solutions consistent with previous findings of aerostats. Mi and Gottlieb (2016) derived a nonlinear initial boundary value problem for a planar multi-tethered spherical aerostat system and observed super-harmonic periodic, period-doubled, quasi-periodic and chaotic-like frequency responses. Mi and Gottlieb (2017) formulated a six-degree of freedom multi-tethered rigid body spherical aerostat system. Their linear stability analysis revealed the existence of a supercritical Hopf bifurcation with respect to the reduced velocity.

Besides the first two periodic modes (modes I and II), Jauvtis et al. (2001) observed another periodic vibration state (mode III) and intermittent bursts of vibrations (mode IV) over the reduced velocity ranges $U^* \in [20, 40]$ and $U^* > 100$, respectively, with high-mass-ratio spheres. Mode III is not a VIV response as the vortex shedding frequency was three to eight times higher than the sphere vibration frequency. Mode IV also not a VIV response, even though it is a flow-induced vibration response. The recent computational study of Rajamuni et al. (2018b) of a tethered sphere, over the Reynolds number range $Re \in [500, 2000]$, claimed that mode III is an intrinsically unstable vibration state that can only be expected for high-inertia

Please cite this article as: M.M. Rajamuni, M.C. Thompson and K. Hourigan, Vortex-induced vibration of elastically-mounted spheres: A comparison of the response of three degrees of freedom and one degree of freedom systems. Journal of Fluids and Structures (2019), https://doi.org/10.1016/j.jfluidstructs.2019.02.005.

Table 1
Non-dimensional parameters. The streamwise direction is parallel to the x–axis, the y and z axis are orthogonal to the flow and referred to as the transverse and lateral directions, respectively. Here, ρ_s and ρ are the densities of solid and fluid, respectively; D is the diameter of the sphere; U is the upstream velocity; ν is the kinematic viscosity of the fluid; f is the sphere vibration frequency; f_n is the natural frequency of the system (without the added mass effect); f_{vo} is the vortex shedding frequency; F_d and F_l are the drag and lift forces, respectively; and $A_{x,rms}$, $A_{y,rms}$ and $A_{z,rms}$ are the r.m.s. of the sphere displacement signals in y and z directions, respectively.

Parameter	Symbol
Mass ratio	$m^* = \rho_s/\rho$
Reynolds number	$Re = DU/\nu$
Reduced velocity	$U^* = U/(Df_n)$
Amplitude ratios	$A_x^* = \sqrt{2}A_{x,rms}/D$
	$A_y^* = \sqrt{2}A_{y,rms}/D$
	$A_z^* = \sqrt{2}A_{z,rms}/D$
Drag coefficient	$C_d = F_d/(2\rho U^2\pi(D/2)^2)$
Lift coefficient	$C_l = F_l/(2\rho U^2\pi(D/2)^2)$
Frequency ratio	$f^* = f/f_n$
Strouhal number	$St = f_{vo}D/U$

spheres. Both Rajamuni et al. (2018a,b) observed mode IV type aperiodic response immediately following the mode II regime, at lower reduced velocities, for small-mass-ratio spheres.

The experimental study of Brücker (1999) examined freely rising air bubbles in water and found three different types of bubble motion: spiralling, zigzagging, and rocking, during their rise. His results showed that zigzagging motion was coupled to the generation of two-sided hairpin loops, while the spiralling bubble created a twisted pair of streamwise vortices that were wound like a helix. The experimental study of Horowitz and Williamson (2010) revealed that a falling sphere always moves without vibration, and a rising sphere vibrates only if its mass ratio was below a critical value. However, they did not observe a helical or spiral trajectory. A series of experimental and computational studies conducted by Magnaudet and Eames (2000) and Mougin and Magnaudet (2001, 2006) observed a bubble rise in the zigzagging path, sometimes followed by a transition to a spiral path. Mougin and Magnaudet (2001) argued that a zigzag path always appears first, as its growth rate is larger than that of the spiral path.

Behara et al. (2011) was the first to examine the vortex-induced vibration of a sphere mounted with elastic support in all three spatial directions. This numerical study was conducted at a Reynolds number of 300 with a sphere of mass ratio $m^* = 3.82$ (reduced mass of 2) over the reduced velocity range $U^* \in [4, 9]$. They observed two distinct VIV responses at the same reduced velocity, which they named as hairpin and spiral modes. In the hairpin mode, the sphere vibrated in a linear path, as hairpin loops were shedding behind the sphere. In the spiral mode, the sphere vibrated in a circular orbit creating a spiralling vortical structure behind the sphere. In each case, they observed a bell-shaped amplitude response curve with a single peak with a maximum amplitude of ≈ 0.25 diameters, which is much smaller than that observed in experimental studies at higher Reynolds numbers. Recently, Behara and Sotiropoulos (2016) extended this study by expanding the reduced velocity range to $0 \leq U^* \leq 13$. They identified that the sphere vibrates with a larger amplitude when it vibrates in a linear path (hairpin mode) compared with a circular orbit (spiral mode). However, the hairpin mode was identified as an unstable state, as it merged with the spiral mode at higher reduced velocities. They also provided some insight on the effects of Reynolds number on VIV over the range $300 \leq Re \leq 1000$, by fixing the reduced velocity at $U^* = 9$. This study revealed that the sphere response was strongly dependent on the Reynolds number.

Govardhan and Williamson (2005) showed that the VIV response of a sphere is (relatively) independent of the Reynolds number in the range $Re \in [2000, 12000]$. However, the recent computational studies of Rajamuni et al. (2018a,b) reported that the VIV response of a sphere highly depends on the Reynolds number for the range $Re \in [300, 2000]$, especially over the mode II range, regardless whether it is an elastically-mounted sphere with 1-DOF or a tethered sphere. Govardhan and Williamson (2005) claimed that the motion of a tethered sphere with 2-DOF and an elastically-mounted sphere with 1-DOF compared well for a similar mass-damping parameter. However, relatively little is known for the VIV of a sphere allowed to move in all three spatial directions. While the studies of Behara et al. (2011) and Behara and Sotiropoulos (2016) explored VIV of an elastically-mounted sphere with 3-DOF, those studies were mainly conducted on low Reynolds number flow. Even though the study of Behara and Sotiropoulos (2016) provides some insight at somewhat larger Reynolds numbers (up to 1000), no clear picture has been drawn at higher Reynolds numbers. Therefore, this study focuses on exploring the nature of the VIV of a sphere, mounted with elastic supports in all three spatial directions, at the Reynolds number of 2000, and to compare the response with the responses of an elastically-mounted sphere whose motion is restricted to the transverse direction (1-DOF) and a tethered sphere. The non-dimensional parameters employed in this study are listed in Table 1.

2. Numerical methodology and validation studies

The CFD package OpenFOAM developed based on a finite volume method was used for the numerical simulations. It is an open-source CFD package released by OpenCFD Ltd for Unix operating systems. This package is capable of solving a

Please cite this article as: M.M. Rajamuni, M.C. Thompson and K. Hourigan, Vortex-induced vibration of elastically-mounted spheres: A comparison of the response of three degrees of freedom and one degree of freedom systems. Journal of Fluids and Structures (2019), https://doi.org/10.1016/j.jfluidstructs.2019.02.005.

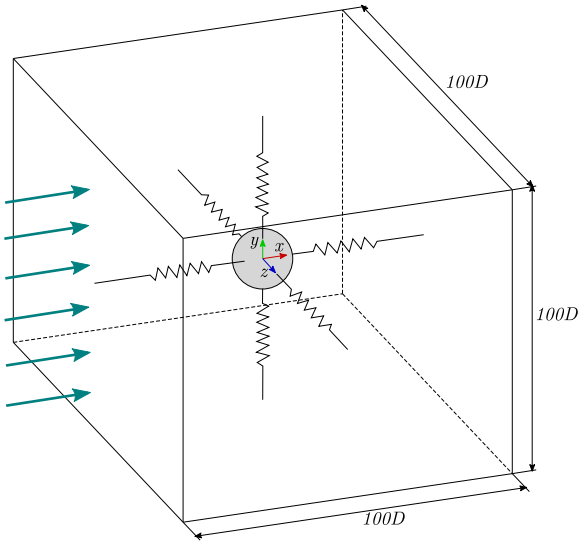

Fig. 1. Schematic of the computational domain, where D is the diameter of the sphere. The flow is in the x direction, and the sphere is allowed to translate in all three spatial directions.

wide variety of flow problems. It also has the capability of performing simulations using multiple processors in parallel. Recent versions of OpenFOAM enable the solution of Fluid–Structure Interaction problems, with the help of dynamic grid techniques. However, these methods are time-consuming and computationally costly, as the grid is deformed according to the solid motion at the end of each time step. Nevertheless, OpenFOAM allows the user to develop their own flow solvers and libraries. We developed a fully-coupled FSI solver in the OpenFOAM framework to efficiently solve flow-induced vibration problems of a single body. Previously, Blackburn and Henderson (1996), Leontini et al. (2006) and Lee et al. (2013) also employed similar approaches in their numerical studies of flow-induced vibration problems. The FSI system and the FSI solver are discussed in detail in the following two subsections.

2.1. Governing equations

To avoid mesh deformation, a moving reference frame attached to the centre of the sphere was used to model the fluid flow. This is a non-inertial reference frame, as its velocity is not fixed. Therefore, the fixed-frame (momentum) Navier–Stokes equations need to be adjusted accordingly, as given in Eq. (1). This can be done by adding the acceleration of the frame, which is indeed the acceleration of the sphere, to the momentum equations, as a source term. The elastically-mounted solid was assumed to be a rigid body, while its motion was assumed to behave as a spring–mass–damper system. The fluid was assumed incompressible, Newtonian and viscous.

The coupled fluid–solid system can be described by the Navier–Stokes equations given by Eq. (1), and the continuity equation given by (2), together with the governing equation for the motion of the sphere by Eq. (3):

$$\frac{\partial \boldsymbol{u}}{\partial t} + (\boldsymbol{u}\cdot\nabla)\boldsymbol{u} \;=\; -\nabla P/\rho \;+\; \nu\,\nabla^2\boldsymbol{u} \;-\; \ddot{\boldsymbol{x}}_{\boldsymbol{s}}, \tag{1}$$

$$\nabla\cdot\boldsymbol{u} \;=\; 0, \tag{2}$$

$$m\,\ddot{\boldsymbol{x}}_{\boldsymbol{s}} \;+\; c\,\dot{\boldsymbol{x}}_{\boldsymbol{s}} \;+\; k\,\boldsymbol{x}_{\boldsymbol{s}} \;=\; \boldsymbol{f}_{\boldsymbol{I}}. \tag{3}$$

Here, $\boldsymbol{u} = \boldsymbol{u}(x, y, z, t)$ is the velocity vector field, P is the scalar pressure field, ρ is the fluid density, and ν is the kinematic viscosity of the fluid, $\boldsymbol{x}_{\boldsymbol{s}}$, $\dot{\boldsymbol{x}}_{\boldsymbol{s}}$, and $\ddot{\boldsymbol{x}}_{\boldsymbol{s}}$ are the sphere displacement, velocity, and acceleration vectors, respectively. In addition, m is the mass of the sphere, c is the damping constant, k is the structural spring constant, and $\boldsymbol{f}_{\boldsymbol{I}}$ is the flow-induced integrated vector force acting on the sphere due to kinematic pressure and viscous shear forces acting on the body surface.

2.2. Fluid-Structure Interaction (FSI) solver

A solver (named vivIcoFoam) was developed to solve the fully-coupled fluid–structure system defined by the Eqs. (1)–(3) for laminar flows. This FSI solver is based on the pre-built *icoFoam* transient solver, which is implemented according to the pressure implicit splitting of operators (PISO) algorithm introduced by Issa (1986). The vivIcoFoam solver employs a predictor–corrector iterative method, which initially predicts the solid motion, and corrects it in several corrector iterations. In particular, the prediction and correction of the solid motion at the $(n+1)$th time step can be elaborate as follows.

Please cite this article as: M.M. Rajamuni, M.C. Thompson and K. Hourigan, Vortex-induced vibration of elastically-mounted spheres: A comparison of the response of three degrees of freedom and one degree of freedom systems. Journal of Fluids and Structures (2019), https://doi.org/10.1016/j.jfluidstructs.2019.02.005.

Table 2
Comparison of computed time-averaged drag coefficient, $\overline{C}_d$, and Strouhal numbers, St-1 and St-2, at $Re = 1000$ with other studies.

Study	$Re = 1000$		
	$\overline{C}_d$	St-1	St-2
Present	0.49	0.19	0.33
Morsi and Alexander (1972)	0.46	–	–
Poon et al. (2014)	0.46	0.185	0.33
Poon et al. (2009)	0.46	0.2	0.34
Roos and Willmarth (1971)	0.472 0.483	–	–
Tomboulides and Orszag (2000)	–	0.2	0.35

At the **predictor iteration**, the acceleration of the solid body is explicitly predicted by a third-order polynomial extrapolation using the values calculated in the previous three time steps by

$$\ddot{\boldsymbol{x}}_s^{(n+1)} = 3\ddot{\boldsymbol{x}}_s^{(n)} - 3\ddot{\boldsymbol{x}}_s^{(n-1)} + \ddot{\boldsymbol{x}}_s^{(n-2)}. \tag{4}$$

At a **corrector iteration**, the solid acceleration is corrected with $\dot{\boldsymbol{x}}_s$, $\boldsymbol{x}_s$, and $\boldsymbol{f}_l$ calculated in the previous iteration by

$$\ddot{\boldsymbol{x}}_s^{(n+1)} = -\frac{c}{m}\left(\dot{\boldsymbol{x}}_s^{(n+1)}\right) - \frac{k}{m}\left(\boldsymbol{x}_s^{(n+1)}\right) + \frac{\boldsymbol{f}_l}{m}. \tag{5}$$

Afterwards, in each iteration, the solid velocity and displacement are calculated, by a third order Adams–Moulton by

$$\dot{\boldsymbol{x}}_s^{(n+1)} = \dot{\boldsymbol{x}}_s^{(n)} + \frac{\delta t}{12}\left(5\ddot{\boldsymbol{x}}_s^{(n+1)} + 8\ddot{\boldsymbol{x}}_s^{(n)} - \ddot{\boldsymbol{x}}_s^{(n-1)}\right) \tag{6}$$

and

$$\boldsymbol{x}_s^{(n+1)} = \boldsymbol{x}_s^{(n)} + \frac{\delta t}{12}\left(5\dot{\boldsymbol{x}}_s^{(n+1)} + 8\dot{\boldsymbol{x}}_s^{(n)} - \dot{\boldsymbol{x}}_s^{(n-1)}\right). \tag{7}$$

At the end of each iteration, the fluid equations given in Eqs. (1) and (2) are solved with the predicted or subsequently corrected solid acceleration, and the fluid forces induced on the solid are calculated. The readers are referred to Rajamuni et al. (2018a,c) for further details of the solver. The iterative process was terminated when the relative error of the magnitudes of the solid acceleration and the fluid forces were less than a given error bound, ϵ. For the present study, $\epsilon = 0.001$ was chosen since it was found that further decreasing ϵ does not increase the accuracy of the solution. As for the fluid solver, the overall vivIcoFoam solver is of second-order temporal accuracy.

The fluid domain was modelled in a moving frame of reference. This motion is acknowledged through the outer domain velocity boundary conditions (except the outlet boundary). In this study, the velocity is prescribed on all the outer boundaries except the outlet. Once the predictor–corrector iterative process has been completed, the velocity at the inlet boundaries is updated according to the velocity of the solid body, $\dot{\boldsymbol{x}}_s$, before proceeding to the next time step.

2.3. Validation studies

The flow past an stationary sphere was investigated at $Re = 1000$ to demonstrate the validity of the numerical method. Table 2 compares the results obtained for the time averaged drag coefficient, $\overline{C}_d$, and Strouhal numbers, $St - 1$ and $St - 2$ with the results of Morsi and Alexander (1972), Poon et al. (2014, 2009), Roos and Willmarth (1971) and Tomboulides and Orszag (2000). As can be seen, the present results closely match values calculated in other studies.

Another set of simulations was conducted with a 2-dimensional cylinder, at the parameters chosen from the numerical study of Leontini et al. (2006), to check the validity of the vivIcoFoam solver developed for VIV problems. The Reynolds number, mass ratio, and the damping ratio were fixed at $Re = 200$, $m^* = 10$, and $\zeta = 0.01$, respectively, while the reduced velocity was varied in the range $U^* \in [3.5,\ 7]$. Fig. 2 compares our results with observations of Leontini et al. (2006) for the cylinder vibration amplitude, A^*, fluctuation amplitude of the lift coefficient, C_l', frequency ratio, f^*, and the phase between the cylinder vibration and the lift force, ϕ. As the figure shows, the results obtained are closely match with the findings of Leontini et al. (2006). This provides validation of the new solver. This solver was also used for the computational study of Rajamuni et al. (2018c) to examine the effect of transverse rotation on the flow-induced vibration of a sphere.

2.4. Computational detail

Fig. 1 shows a schematic of the fluid–structure system used for the simulations presented in this paper. A cubic domain with a side length of $100D$ was chosen for the fluid, and the sphere was placed at the centre of it. As shown in the figure, the sphere was mounted with elastic supports, allowing to translate in all three spatial directions. The stiffness of the springs was assumed to be identical in all three directions. To examine the nature of the VIV, a range of reduced velocities was obtained

Please cite this article as: M.M. Rajamuni, M.C. Thompson and K. Hourigan, Vortex-induced vibration of elastically-mounted spheres: A comparison of the response of three degrees of freedom and one degree of freedom systems. Journal of Fluids and Structures (2019), https://doi.org/10.1016/j.jfluidstructs.2019.02.005.

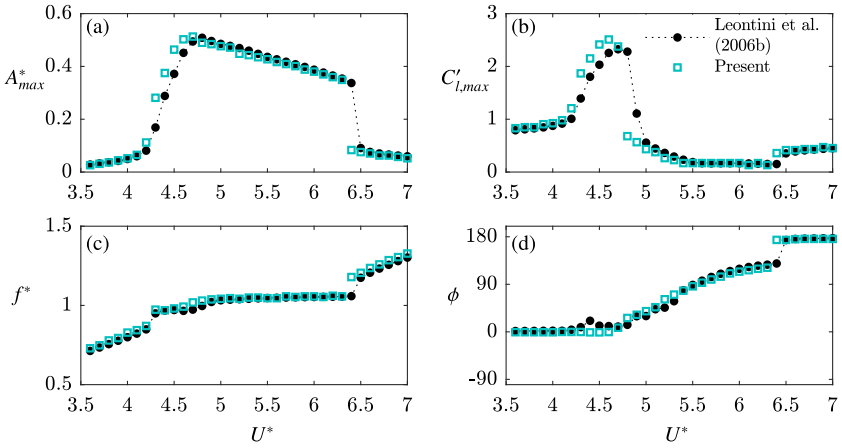

Fig. 2. Comparison of the VIV response of a cylinder at $Re = 200$, $m^* = 10$, and $\zeta = 0.01$ with the results of Leontini et al. (2006). (a) Maximum vibration amplitude, A^*_{max}; (b) peak lift coefficient, $C'_{l,max}$; (c) frequency ratio, $f^* = f/f_n$; and (d) average phase between the sphere vibration and the lift force, ϕ in degrees.

Table 3
Boundary conditions: U is the upstream velocity; $\boldsymbol{\eta}$ is the outward normal vector at a corresponding boundary; and $\dot{\boldsymbol{x}}_s$ is the velocity of the sphere.

Boundary	Velocity, $\boldsymbol{u}$	Pressure, p
Inlet	$\boldsymbol{u} = (U\ 0\ 0) - \dot{\boldsymbol{x}}_s$	$\nabla p \cdot \boldsymbol{\eta} = 0$
Sphere	$\boldsymbol{u} = (0\ 0\ 0)$	$\nabla p \cdot \boldsymbol{\eta} = 0$
Outlet	$\nabla \boldsymbol{u} \cdot \boldsymbol{\eta} = 0$	$p = 0$

Table 4
The sensitivity of the spatial resolution of the flow parameters of VIV of a sphere at $Re = 2000$, $U^* = 7$, and $m^* = 3$. Here, N_r is the number of cells in the radial direction of a square frustum and N_t is the number of cells on the sphere surface. The r.m.s. value of the sphere response amplitude ratios in y and z directions, A^*_y and A^*_z, respectively, the time-averaged drag coefficient, $\overline{C}_d$, the r.m.s. value of the drag coefficient, $C_{d,rms}$, and the frequency ratio, f^*, are listed.

Grid	N_r	N_t	# Cells	A^*_y	A^*_z	$\overline{C}_d$	$C_{d,rms}$	f^*
Grid 1	50	7 350	0.83×10^6	0.53	0.54	0.90	0.05	0.98
Grid 2	100	7 350	1.20×10^6	0.54	0.54	0.88	0.04	0.98
Grid 3	150	7 350	1.57×10^6	0.55	0.54	0.89	0.04	0.98
Grid 4	200	7 350	1.94×10^6	0.54	0.55	0.89	0.04	0.98
Grid 5	100	12 150	1.88×10^6	0.54	0.53	0.88	0.04	0.98
Grid 6	100	18 150	2.71×10^6	0.54	0.53	0.88	0.04	0.98
Grid 7	100	25 350	3.70×10^6	0.53	0.53	0.88	0.04	0.98

by varying the spring constant, k, according to the relation $U^* = 2\pi\sqrt{m/k}\ U/D$. In the present study, the motion of the sphere was considered as a spring–mass system with zero damping constant, to achieve the maximum possible oscillation amplitude.

Table 3 shows the boundary conditions applied at the inlets, outlet, and sphere boundaries. Five inlet faces of the cubic fluid domain have velocity prescribed on them, with the zero-gradient pressure condition. The downstream side of the cubic domain is an outlet with zero pressure. The sphere boundary was treated as a wall and assumed to satisfy the no-slip condition. The upstream flow (in the fixed frame) was taken to be aligned with x direction, as indicated in Fig. 1.

2.5. The computational grid and resolution study

Ansys-ICEM-CFD was used to generate a hexahedral cell grid for the fluid domain. The grid was created such that it was concentrated towards the sphere surface. To achieve this, a cubic block, with a side length of $5D$, was placed around the sphere. This block was decomposed into small cells with uniformly distributed nodes in the tangential directions, and exponentially distributed nodes in the radial direction. A large number of cells were assigned in the downstream direction to resolve the wake structures behind the sphere. For more detail of the grid structure, please refer to Rajamuni et al. (2018a). A series of finer grids were generated by changing the number of cells in the radial and tangential directions, N_r and N_t, respectively, to observe the sensitivity of the computed solution on the spatial resolution. In each grid, the minimum cell thickness in the radial direction was fixed at $0.002D$. The VIV response of the sphere was examined at $Re = 2000$, $U^* = 7$,

Please cite this article as: M.M. Rajamuni, M.C. Thompson and K. Hourigan, Vortex-induced vibration of elastically-mounted spheres: A comparison of the response of three degrees of freedom and one degree of freedom systems. Journal of Fluids and Structures (2019), https://doi.org/10.1016/j.jfluidstructs.2019.02.005.

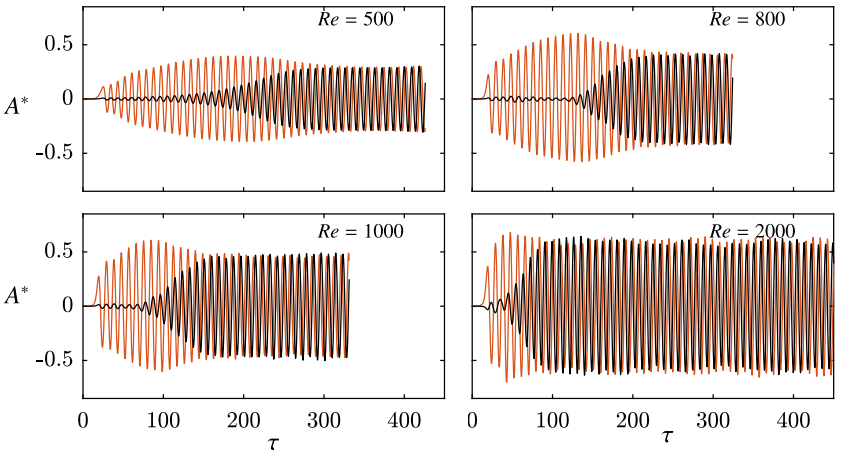

Fig. 3. Time histories of the sphere response amplitudes against the non-dimensional time, $\tau = tU/D$ at $U^* = 9$ and $Re = 500$, 800, 1000 and 2000. The amplitudes in the transverse direction (y) are shown by the orange (light) curve, while the amplitudes in the lateral direction are shown by the black (dark) curve. At each case, the sphere initially vibrates linearly in the transverse direction, and eventually, it vibrates in a circular orbit orthogonal to the flow. (For interpretation of the references to colour in this figure legend, the reader is referred to the web version of this article.)

and $m^* = 3$ with the sequence of grids. For these parameter values, the sphere was found to vibrate in a circular orbit with nearly equal amplitudes in both y and z directions. Table 4 compares the effect of grid refinement on the results for sphere response amplitudes, A_y^* and A_z^*; time-averaged and fluctuating drag coefficient, $\overline{C}_d$ and $C_{d,rms}$, respectively, and the frequency ratio, f^*. As can be seen, the results obtained from grids 2–7 are in a good agreement with one another, with less than 2% variation in the prediction. Grid 2 was used to obtain all the results presented in this paper, as the increment of N_r or N_t only affected the prediction weakly. The time step used for all of the simulations presented in this paper was $0.005U/D$, corresponding to approximately 1000 timesteps more per shedding period.

3. Results

3.1. The sphere response for varying Reynolds numbers

Vortex-induced vibration of a sphere allowed to translate in all three spatial directions was examined over the Reynolds number range $Re \in [300, 2000]$ with a sphere of mass ratio $m^* = 3.82$ (equivalent to the reduced mass of 2 used by Behara et al. (2011) and Behara and Sotiropoulos (2016)), by fixing the reduced velocity at $U^* = 9$. These m^* and U^* values were chosen for the present study, to later compare the predictions with those of Behara and Sotiropoulos (2016), who examined the effect of Re for the same parameter values. At each Reynolds number, the sphere initially commenced to vibrate in the transverse direction, synchronized with alternatively shed vortex loops from the opposite sides of the sphere. However, the sphere gradually began to vibrate in the lateral (z) direction as time progressed. In its asymptotic state, the vibration amplitudes in both transverse and lateral directions became nearly (effectively) equal, with the sphere orbiting in a circular trajectory orthogonal to the flow.

On one hand, the present results match well with the findings of Mougin and Magnaudet (2001), who examined the path of rising bubbles. Mougin and Magnaudet (2001) found a freely rising bubble that initially followed a zigzag motion, sometimes transitioned to a circular helix motion. In the literature on rising bubbles, the zigzag motion was always observed first and then the helix motion, but not vice verse. Mougin and Magnaudet (2006) extended the study of Mougin and Magnaudet (2001) by examining the wake-induced forces and torques experienced by the bubble. They revealed that the wake-induced effects are balanced by added-mass effects to enable the existence of both zigzag and helical motions. On the other hand, the present results are somewhat different from the findings of Behara et al. (2011) and Behara and Sotiropoulos (2016), who observed two different sphere responses (linear and spiral) for the same reduced velocities at $Re = 300$.

Fig. 3 shows time histories of the vibration amplitude in the transverse and lateral directions at four different Reynolds numbers. Consistent with the observation of Mougin and Magnaudet (2001), the sphere vibration amplitude reduced as it transitioned from a linear path to a circular orbit. Behara and Sotiropoulos (2016) also observed a larger amplitude for the hairpin mode than for the spiral mode. At low Reynolds numbers, it takes a long time for the vibrations to grow in amplitude towards the asymptotic state. At $Re = 300$, the response neared the asymptotic state around non-dimensional time $\tau \approx 550$ (not shown in the graph). However, as the Reynolds number increased, the transition time shortened and the sphere quickly began to vibrate in a circular orbit. Moreover, the sphere vibration was purely sinusoidal at lower Reynolds number, but it was slightly less sinusoidal at higher Reynolds numbers, as a result of the wake becoming more complex.

The wake behind the sphere was visualized using the Q-criterion. Fig. 4 shows the wake structures observed at the initial and final states for $Re = 500$, 1000 and 2000. In the initial state, two trails of interlaced hairpin vortex loops were found in

Please cite this article as: M.M. Rajamuni, M.C. Thompson and K. Hourigan, Vortex-induced vibration of elastically-mounted spheres: A comparison of the response of three degrees of freedom and one degree of freedom systems. Journal of Fluids and Structures (2019), https://doi.org/10.1016/j.jfluidstructs.2019.02.005.

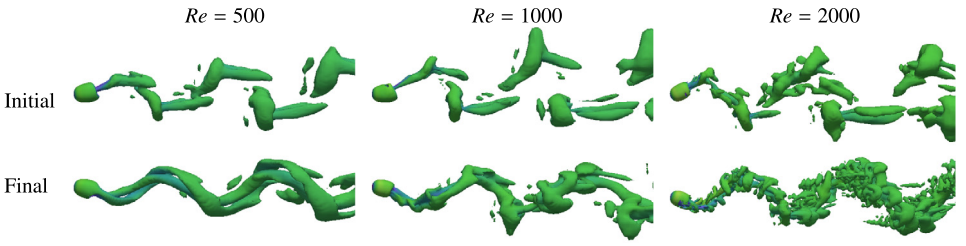

Fig. 4. Wake structures observed at the initial and final stages of the sphere vibration at $Re = 500$, 1000, and 2000. The wake structures were visualized by the Q-criterion ($Q = 0.001$). Flow is from left to right.

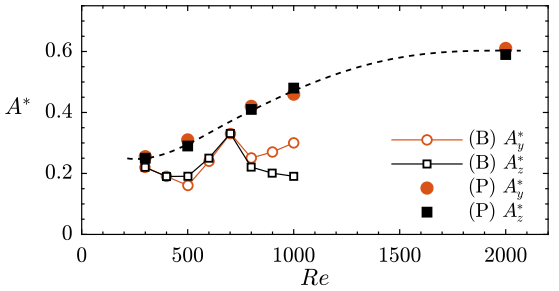

Fig. 5. The sphere response amplitudes (A_y^*–transverse and A_z^*–lateral) as a function of Reynolds number. The solid symbols (marked as P) are the current results, while the hollow symbols (marked as B) are the results of Behara and Sotiropoulos (2016).

the wake, as the sphere vibrates along a linear path. In the final state, a spiralling wake was found behind the sphere, as it vibrates in a circular orbit. The wake structures we observed at $Re = 500$ in the initial and final states, strongly resemble the observations of Behara et al. (2011) at their hairpin and spiral modes, respectively. The wake is modified with the addition of small-scale structures, as the Reynolds number is increased, especially in the final state.

Fig. 5 compares the sphere response amplitude with that observed by Behara and Sotiropoulos (2016) for the Reynolds number range $Re \in [300, 2000]$. As can be seen, the sphere response amplitude was found to increase with increasing Reynolds number. In comparison with our results, Behara and Sotiropoulos (2016) observed relatively smaller amplitudes in both the transverse and lateral directions. In addition, they reported various sphere responses depending on the Reynolds number, while the sphere was found to always move in a circular orbit in its asymptotic state in the present study. It is perhaps possible that the asymptotic state was not reached in the simulations of Behara and Sotiropoulos (2016).

3.2. The sphere response at $Re = 2000$

Vortex-induced vibration of an elastically-mounted sphere was examined for a sphere of mass ratio $m^* = 3$, over the reduced velocity range $3.5 \leq U^* \leq 16$, by fixing the Reynolds number at $Re = 2000$. Two sets of simulations were conducted: in one case, the sphere was allowed to translate in all three spatial directions, and in the other case, the sphere motion was restricted to only move in the transverse direction.

When the sphere is mounted with elastic supports in all three spatial directions, it was excited to vibrate beyond $U^* = 4$, and it showed synchronized vibrations up to the highest reduced velocity considered ($U^* = 16$). In each case, the sphere initially vibrated in a linear path and eventually it transitioned to a circular orbit, as observed for different Reynolds numbers at $U^* = 9$. Fig. 6 clearly indicates this transition by plotting the absolute value of the sphere displacement in the y–z plane, $|A_{yz}^*|$, versus non-dimensional time, for $U^* = 7$, 9, 11, and 13. In each case, $|A_{yz}^*|$ highly oscillates until $\tau \approx 150$ and beyond that it remains almost constant with a small variation, as the sphere vibrates in a circular orbit.

Fig. 7 shows the variation of the sphere response amplitudes in the streamwise (x), transverse (y) and lateral (z) directions, over the reduced velocity range $3.5 \leq U^* \leq 16$, when the sphere was allowed to translate in all three spatial directions. The sphere vibrated with large and nearly equal amplitudes in the transverse and lateral directions, while it showed a negligible amplitude ($A^* < 0.03$) in the streamwise direction. Over the entire U^* range investigated, the vibration can be classified as vortex-induced vibration, where the sphere vibrates at the vortex shedding frequency, f_{vo}, and close to the natural frequency of the system (see Fig. 8(b)).

The periodicity of the sphere vibration, λ_A, was obtained by the ratio between the r.m.s. amplitude and the maximum amplitude. In particular, $\lambda_{A,y} = \sqrt{2}A_{y,rms}/A_{y,max}$ and $\lambda_{A,z} = \sqrt{2}A_{z,rms}/A_{z,max}$ are the periodicities of the sphere response in the transverse and lateral directions, respectively. According to these definitions, the periodicity takes values between 0 and 1, where $\lambda_A = 1$ represent the sinusoidal response. As Fig. 8(c) shows, all of the synchronized vibrations were highly periodic

Please cite this article as: M.M. Rajamuni, M.C. Thompson and K. Hourigan, Vortex-induced vibration of elastically-mounted spheres: A comparison of the response of three degrees of freedom and one degree of freedom systems. Journal of Fluids and Structures (2019), https://doi.org/10.1016/j.jfluidstructs.2019.02.005.

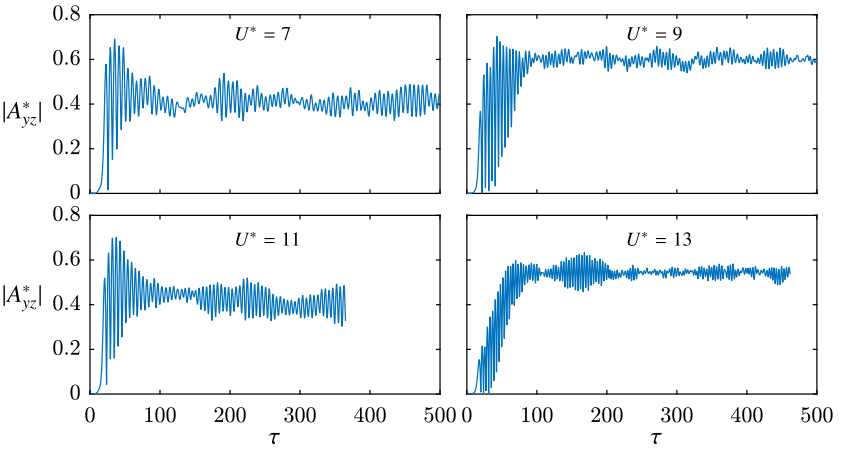

Fig. 6. Absolute value of the sphere displacement in the y–z plane, $|A^*_{yz}|$, as a function of non-dimensional time, τ, at $Re = 2000$ for $U^* = 7$, 9, 11, and 13.

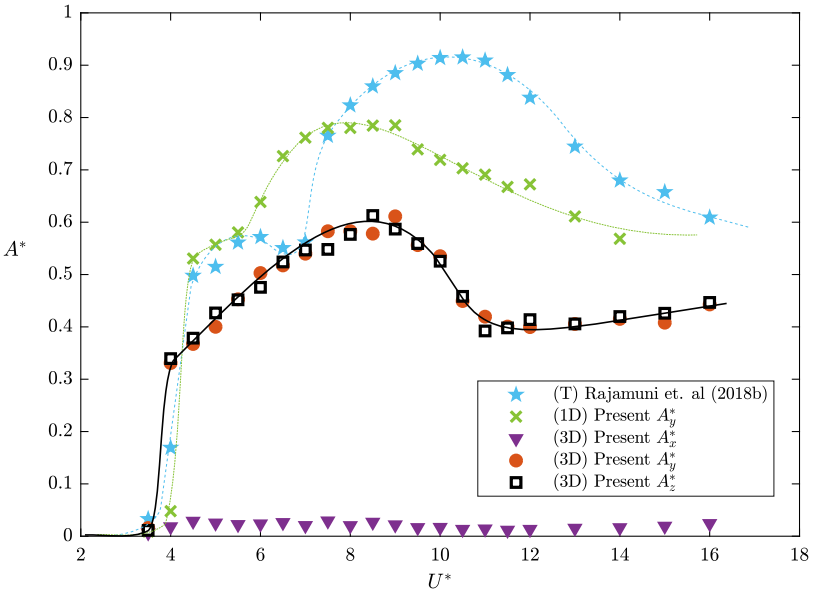

Fig. 7. Comparison of the sphere response amplitude curves at $Re = 2000$ for three different mounting methods; 3D – a sphere of $m^* = 3$ mounted with elastic supports in all three spatial directions: 1D – elastically-mounted sphere of $m^* = 3$ whose motion is restricted to the transverse (y) direction; and T– results of Rajamuni et al. (2018b) with a tethered sphere of $m^* = 0.8$. Here, A^*_x, A^*_y and A^*_z are the amplitudes in the streamwise, transverse and lateral directions, respectively.

in both the transverse and lateral directions, similar to the highly periodic mode I and II vibrations observed by Williamson and Govardhan (1997), Govardhan and Williamson (1997, 2005), Jauvtis et al. (2001), Rajamuni et al. (2018a,b), and the highly periodic synchronized vibrations observed by van Hout et al. (2010), Behara et al. (2011) and Lee et al. (2013) for both tethered and elastically-mounted spheres. The sphere trajectories at five reduced velocities ($U^* = 5$, 7, 9, 11 and 15) in the y–z plane are shown in Fig. 9. As can be seen, the sphere vibrated in a circular orbit in a plane orthogonal to the flow.

Fig. 7 also compares the response of an elastically-mounted sphere with 3-DOF with the response of an elastically-mounted sphere whose motion is restricted to the transverse (y) direction. Even though the sphere showed highly periodic vibrations in each case, it vibrated with a larger amplitude when the motion was restricted to the transverse direction compared to the 3-DOF motion. Allowing the sphere to move in all spatial directions seems to reduce the vibration amplitude as it vibrates in a circular orbit compared to a linear path under 1-DOF motion. Consistently, the studies of Behara et al. (2011) and Behara and Sotiropoulos (2016) with an elastically-mounted sphere of 3-DOF at $Re = 300$ observed a smaller amplitude when the sphere moved in a circular orbit (spiral mode) than when it moved along a linear path (hairpin mode).

Govardhan and Williamson (2005) compared the motion of an elastically-mounted sphere free to move only in the transverse direction with the motion of a tethered sphere allowing 2-DOF (xy motion). They also observed that the sphere

Please cite this article as: M.M. Rajamuni, M.C. Thompson and K. Hourigan, Vortex-induced vibration of elastically-mounted spheres: A comparison of the response of three degrees of freedom and one degree of freedom systems. Journal of Fluids and Structures (2019), https://doi.org/10.1016/j.jfluidstructs.2019.02.005.

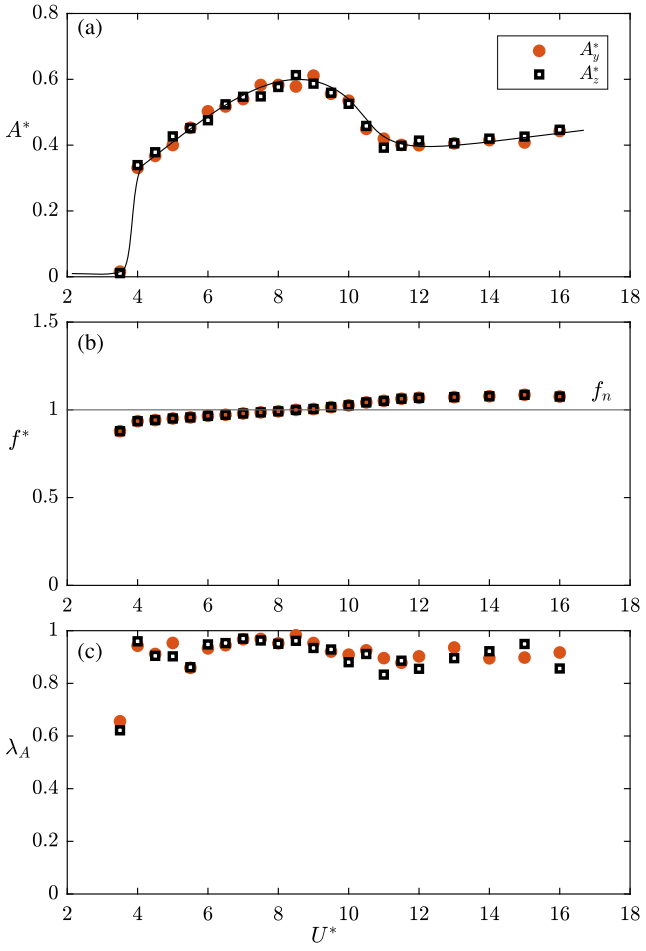

Fig. 8. The vortex-induced vibration response of a sphere with 3-DOF at $Re = 2000$ and $m^* = 3$ over the reduced velocity range $3.5 \leq U^* \leq 16$: (a) the sphere response amplitudes A_y^* and A_z^*; (b) the frequency ratios f_y^* and f_z^*; and (c) the periodicities of the sphere vibration $\lambda_{A,y}$ and $\lambda_{A,z}$. Here, the symbols ● and □ represents the quantities calculated with the transverse (y) and lateral (z) components of the sphere response.

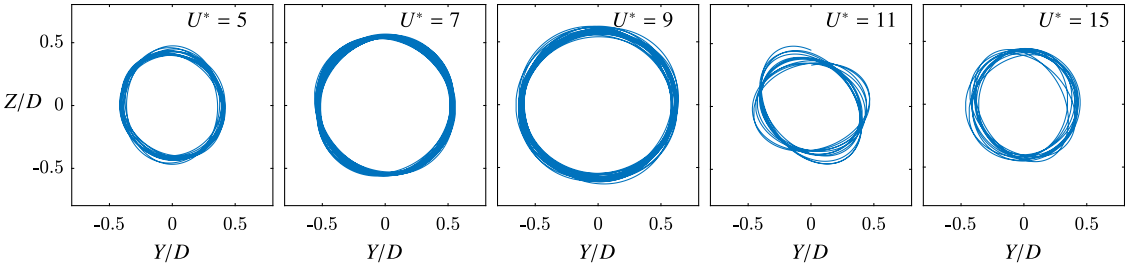

Fig. 9. The sphere trajectories in the y–z plane at $Re = 2000$, $m^* = 3$ and $U^* = 5$, 7, 9, 11 and 15.

vibrates with a slightly larger amplitude when the motion is restricted to the transverse direction. Moreover, they claimed that the motion of the tethered sphere and a hydroelastic sphere (y only) compare well for the same mass damping parameter, as they observed similar response curves. Nevertheless, the shape of the amplitude response curve when the sphere is allowed to translate in all three spatial directions (3-DOF) differs from that of a sphere allowed to move only in the transverse direction (1-DOF), as Fig. 7 shows. The response curve for 1-DOF shows a local peak in mode I beside the global peak in mode II. However, the response curve for 3-DOF motion has only a single peak around $U^* = 8.5$, and the amplitude shows a slightly increasing trend beyond the peak for $U^* > 11$. No clear indication of modes I and II was visible from the amplitude response curve. However, the analysis of force measurements revealed that the sphere shows mode I

Please cite this article as: M.M. Rajamuni, M.C. Thompson and K. Hourigan, Vortex-induced vibration of elastically-mounted spheres: A comparison of the response of three degrees of freedom and one degree of freedom systems. Journal of Fluids and Structures (2019), https://doi.org/10.1016/j.jfluidstructs.2019.02.005.

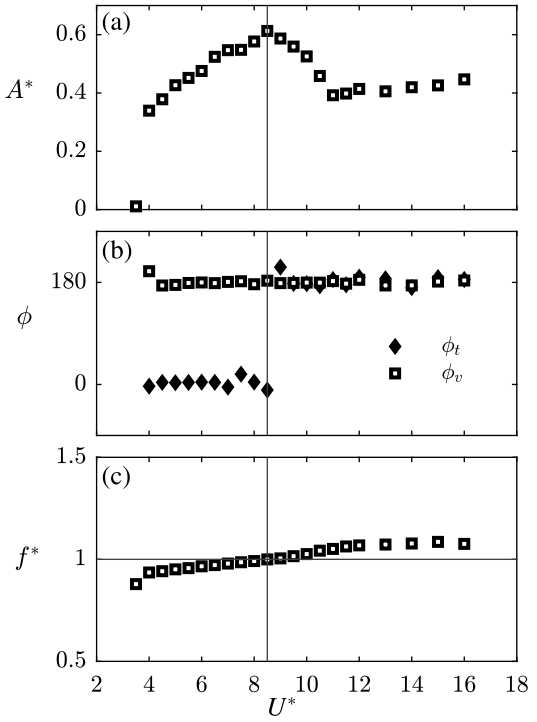

Fig. 10. Variation of the total phase, ϕ_t, and the vortex phase, ϕ_v, over the reduced velocity range $4 \leq U^* \leq 16$. The total phase shift from 0° to 180° as the frequency ratio crosses the $f^* = 1$ line around $U^* = 8.5$. This figure was generated with the lateral components of the sphere response and the lift force. A similar observation was found for the traverse component as well.

type response up to $U^* = 8.5$ and mode II type response for $U^* > 8.5$, albeit it is moving in a circular orbit when mounted with elastic supports in all three spatial directions.

Fig. 7 also plots the response curve of a tethered sphere observed by Rajamuni et al. (2018b) at the same Reynolds number, with a sphere of mass ratio $m^* = 0.8$. The response of the tethered sphere compares well with the elastically-mounted sphere of 1-DOF rather than with the elastically-mounted sphere of 3-DOF. Both tethered spheres and those elastically-mounted in the transverse direction vibrated with identical amplitudes in mode I. However, the tethered sphere showed significantly larger amplitudes over the mode II range. This may be because of the relatively small mass ratio of the tethered sphere.

3.2.1. Force measurements

Previous experimental and numerical studies revealed that a tethered sphere or a sphere elastically-mounted in the transverse direction shows two different VIV modes (namely, modes I and II). Govardhan and Williamson (2005) and Rajamuni et al. (2018a,b) studied the differences between these two modes by analysing the phase between the sphere vibration and the lift force. The *total force* acting on the sphere, F_t, can be conveniently split into two components; a *potential force* component, F_p, related to the potential added mass and a *vortex force* component, F_v, related to the dynamic vorticity, as suggested by Lighthill (1986). The study of Govardhan and Williamson (2000) on the VIV of a cylinder observed a shift in the total phase, ϕ_t (the phase between the total force and the body displacement) or the vortex force, ϕ_v (the phase between the vortex force and the body displacement), as the cylinder motion transitioned between two branches. Consistently, Govardhan and Williamson (2005) and Rajamuni et al. (2018a,b) observed a shift in ϕ_v, as the sphere transitioned from mode I to mode II.

For the case of an elastically-mounted sphere with 3-DOF motion, the existence of different modes of vibrations has not been studied. Moreover, the sphere response curve we observed at $Re = 2000$ and the response curves observed by Behara et al. (2011) and Behara and Sotiropoulos (2016) at $Re = 300$ provide no evidence on different modes of vibrations, as each response curve has only a single peak. However, the transition between modes I and II is smooth for a sphere, and the amplitude response curve does not necessarily have a peak at mode I, especially for elastically-mounted spheres and high-mass ratio spheres (Govardhan and Williamson, 2005; Rajamuni et al., 2018a,b). Therefore, we analysed the variation of ϕ_t and ϕ_v with the reduced velocity, to investigate whether a sphere with 3-DOF motion shows different modes of vibration, analogous to previously determined vibration modes. We found that the total phase shifted from 0° to 180° around $U^* = 8.5$, while the vortex phase remained at 180° throughout the synchronization regime, as Fig. 10(b) shows. Based on this analysis,

Please cite this article as: M.M. Rajamuni, M.C. Thompson and K. Hourigan, Vortex-induced vibration of elastically-mounted spheres: A comparison of the response of three degrees of freedom and one degree of freedom systems. Journal of Fluids and Structures (2019), https://doi.org/10.1016/j.jfluidstructs.2019.02.005.

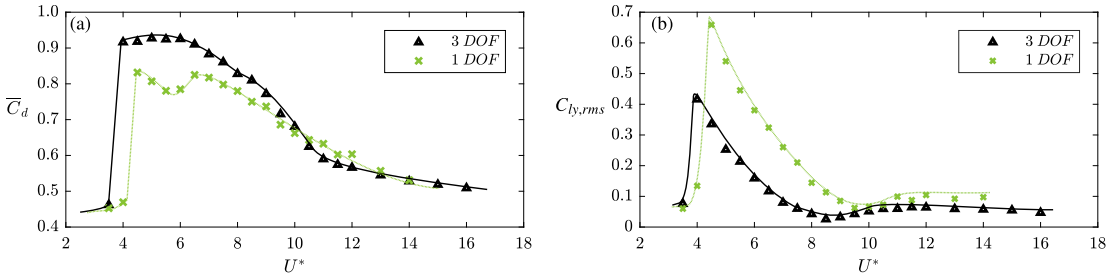

Fig. 11. Plots of (a) the time-averaged drag coefficient, $\overline{C}_d$, and (b) the fluctuation component of the lift force in the y direction as a function of reduced velocity. The symbol $\triangle$ represent the values calculated when the sphere was allowed to move in all three spatial directions and the symbol $\times$ represent when the sphere motion was restricted to the transverse direction.

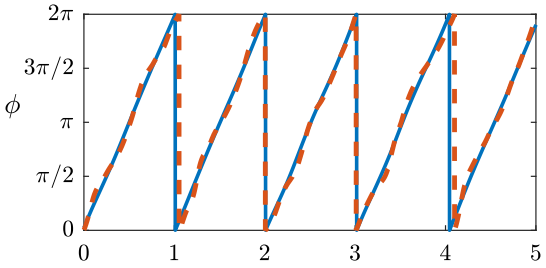

Fig. 12. Comparison of the direction of the sphere (solid blue colour line) and the direction of the fluid forces applied on the sphere (dashed red colour line) in y–z plane for five oscillation cycles of 3-DOF configuration. The sphere vibrates synchronously with the lift forces applied on it.

the sphere showed two different modes of vibrations similar to modes I and II. As Fig. 10(c) shows, the shift of ϕ_t occurs as f^* crosses the $f^* = 1$ line, consistent with the finding of Govardhan and Williamson (2000).

Fig. 11(a) and (b) compares the variation of time-averaged drag coefficient, $\overline{C}_d$, and the fluctuation amplitude of the lift coefficient in the y direction, $C_{ly,rms}$, when the sphere was allowed to have 3-DOF and 1-DOF motion. In each case, the drag coefficient increased suddenly as the sphere began to vibrate, similar to the previous experimental and computations findings. At the beginning of the synchronization regime, $\overline{C}_d$ was nearly doubled when 3-DOF motion was allowed for the sphere. Moreover, the increment of $\overline{C}_d$ from the value observed for a stationary sphere was significantly higher when the sphere vibrated in a circular orbit (3-DOF) than when it vibrated along a linear path (1-DOF). The time-mean lift coefficient was negligible in each case, as the Reynolds number of the flow was 2000. The fluctuation amplitude of the lift coefficient was also found to increase as the synchronized vibration commenced, in each case. A smaller increment in $C_{l,rms}$ was found for the 3-DOF case than for the 1-DOF case. This is consistent with the comparatively smaller response amplitude observed for the 3-DOF case. Interestingly, for the 3-DOF case, the sphere vibrated with a maximum amplitude when the $C_{l,rms}$ was minimum at $U^* = 8.5$.

In the case of 3-DOF, the lift forces applied on the sphere in the y–z plane was compared with the sphere vibration in the y–z plane. The directions of the sphere and the forces in the y–z plane were compared for five oscillation cycles, T_c, as shown in Fig. 12 at $Re = 2000$, and $U^* = 5$. The sphere clearly vibrated in synchrony with the direction of the forces applied on it.

4. Conclusions

The nature of the vortex-induced vibration of an axisymmetric body has been less understood, compared with VIV of a cylindrical body, perhaps partially due to the increased complexity of setting up such an arrangement both experimentally and computationally. Therefore, this numerical study aims to enhance knowledge of VIV of an elastically-mounted spherical body. A series of simulations were conducted using a sphere mounted with elastic supports in all three spatial directions over the reduced velocity range $3.5 \leq U^* \leq 16$, by fixing the mass ratio and the Reynolds number at $m^* = 3$ and $Re = 2000$, respectively. The sphere response, force measurements and the wake behind the sphere were examined and compared with an elastically-mounted sphere whose motion was restricted to the transverse direction over the same parameter set. The major findings of this study can be summarized as follows.

The sphere vibrates in a circular orbit orthogonal to the flow when it is allowed to have 3 *DOF*. When the sphere was mounted with elastic supports in all three spatial directions, initially it was excited to vibrate along a linear path in the transverse direction synchronized with the hairpin vortex loops shed behind the sphere. Gradually, it began to vibrate in the lateral direction as well, presumably assisted by loss of centerplane mirror symmetry of the wake (Mittal, 1999). In the asymptotic state, the sphere vibration amplitudes in both the transverse and lateral directions were nearly equal, leading the sphere

Please cite this article as: M.M. Rajamuni, M.C. Thompson and K. Hourigan, Vortex-induced vibration of elastically-mounted spheres: A comparison of the response of three degrees of freedom and one degree of freedom systems. Journal of Fluids and Structures (2019), https://doi.org/10.1016/j.jfluidstructs.2019.02.005.

to orbit in a circular trajectory orthogonal to the flow. The transition time was found to increase with decreasing Reynolds number for the range $Re \in [300, 2000]$. In the literature of rising bubbles, a transition from a zigzagging path to a helical path has been observed for some parameter sets, similar to the present findings. In addition, the finding of a circular trajectory at high Reynolds number is consistent with the observations of Lee et al. (2013) for a tethered neutrally buoyant sphere.

The sphere vibrates with the smallest amplitude when mounted with elastic supports in all three spatial directions. The sphere was found to show a highly periodic VIV response over the range $4 \leq U^* \leq 16$ when allowed to translate in all three spatial directions. As the sphere vibrated in a circular orbit when 3 *DOF* motion was allowed, its vibration amplitude was significantly smaller than that of a sphere whose motion was restricted to the transverse direction only. The maximum amplitude observed with 3-DOF was ≈ 0.6 diameters while it was ≈ 0.8 diameters with 1-DOF. With similar parameters, a tethered sphere shows the largest vibration amplitude ($0.9 \sim 1.0$ diameters) although this was for a lower mass ratio. With these observations, we can draw the following conclusion. The nature of the VIV response of a sphere strongly depends on the mounting method (elastically mounted or tethered) and the degrees of freedom allowed when mounted with elastic supports. In particular, when 3-DOF motion is allowed to a elastically mounted sphere, it vibrates in a circular orbit and its vibration amplitude is significantly lower than that of a sphere whose motion is restricted to the transverse direction. However, a tethered sphere has 3-DOF and mostly it vibrates along a linear path, similar to a 1-DOF elastically mounted sphere.

The drag coefficient is almost doubled with synchronized vibrations. The time-averaged drag coefficient was found to increase by roughly 100% at the beginning of the synchronization regime for the 3 *DOF* sphere, similar to the observations of Williamson and Govardhan (1997) and Rajamuni et al. (2018b) for tethered spheres. However, the increment of the drag coefficient was significantly smaller for an elastically-mounted sphere whose motion was restricted to the transverse direction (approximately 76%).

A helical wake is formed behind the sphere when it orbits in a circular path. At the initial stage of the sphere vibration, two trails of hairpin loops form the wake. This wake was modified and turned into a helical structure as the sphere transitioned to a circular orbit. The structure of this helical wake was found to depend on the Reynolds number of the flow. Two vortex tubes were present at low Reynolds number; one vortex tube was wound around the other one, strongly resembling the wake observed by Behara et al. (2011) for their spiral mode. At relatively high Reynolds numbers, there was only one major vortex tube, combined with small-scale structures that spiralled synchronously with the sphere vibration.

Based on the above discussion, we can draw the following general observation: the VIV response of a sphere is strongly dependent on the mounting method; in particular, when it is mounted with elastic supports in all three spatial directions, the nature of the response is considerably different to that of a tethered sphere or a sphere elastically-mounted in the transverse direction only.

Acknowledgements

The support from Australian Research Council Discovery Grants DP150102879 and DP170100275, and computing time from the National Computational Infrastructure (NCI) and the Pawsey Supercomputing Centre through merit grants n67 and d71 are gratefully acknowledged.

References

Bearman, P.W., 1984. Vortex shedding from oscillating bluff bodies. Annu. Rev. Fluid Mech. 16, 195–222.
Behara, S., Borazjani, I., Sotiropoulos, F., 2011. Vortex-induced vibrations of an elastically mounted sphere with three degrees of freedom at Re= 300: hysteresis and vortex shedding modes. J. Fluid Mech. 686, 426–450.
Behara, S., Sotiropoulos, F., 2016. Vortex-induced vibrations of an elastically mounted sphere: The effects of Reynolds number and reduced velocity. J. Fluids Struct. 66, 54–68.
Blackburn, H., Henderson, R., 1996. Lock-in behavior in simulated vortex-induced vibration. Exp. Therm Fluid Sci. 12, 184–189.
Brücker, C., 1999. Structure and dynamics of the wake of bubbles and its relevance for bubble interaction. Phys. Fluids (1994-present) 11, 1781–1796.
Constantinescu, G.S., Squires, K.D., 2000. LES and DES Investigations of Turbulent Flow Over a Sphere. American Institute of Aeronautics and Astronautics.
Ern, P., Risso, F., Fabre, D., Magnaudet, J., 2012. Wake-induced oscillatory paths of bodies freely rising or falling in fluids. Annu. Rev. Fluid Mech. 44, 97–121.
Govardhan, R., Williamson, C.H.K., 1997. Vortex-induced motions of a tethered sphere. J. Wind Eng. Ind. Aerodyn. 69, 375–385.
Govardhan, R., Williamson, C.H.K., 2000. Modes of vortex formation and frequency response of a freely vibrating cylinder. J. Fluid Mech. 420, 85–130.
Govardhan, R.N., Williamson, C.H.K., 2005. Vortex-induced vibrations of a sphere. J. Fluid Mech. 531, 11–47.
Horowitz, M., Williamson, C.H.K., 2010. The effect of Reynolds number on the dynamics and wakes of freely rising and falling spheres. J. Fluid Mech. 651, 251–294.
van Hout, R., Katz, A., Greenblatt, D., 2013. Time-resolved particle image velocimetry measurements of vortex and shear layer dynamics in the near wake of a tethered sphere. Phys. Fluids 25, 077102.
van Hout, R., Krakovich, A., Gottlieb, O., 2010. Time resolved measurements of vortex-induced vibrations of a tethered sphere in uniform flow. Phys. Fluids 22, 087101.
Issa, R.I., 1986. Solution of the implicitly discretised fluid flow equations by operator-splitting. J. Comput. Phys. 62, 40–65.
Jauvtis, N., Govardhan, R., Williamson, C.H.K., 2001. Multiple modes of vortex-induced vibration of a sphere. J. Fluids Struct. 15, 555–563.
Lee, H., Hourigan, K., Thompson, M.C., 2013. Vortex-induced vibration of a neutrally buoyant tethered sphere. J. Fluid Mech. 719, 97–128.
Leontini, J.S., Thompson, M.C., Hourigan, K., 2006. The beginning of branching behaviour of vortex-induced vibration during two-dimensional flow. J. Fluids Struct. 22, 857–864.
Lighthill, J., 1986. Wave loading on offshore structures. J. Fluid Mech. 173, 667–681.
Magnaudet, J., Eames, I., 2000. The motion of high-Reynolds-number bubbles in inhomogeneous flows. Annu. Rev. Fluid Mech. 32, 659–708.
Mi, L., Gottlieb, O., 2015. Asymptotic model-based estimation of a wake oscillator for a tethered sphere in uniform flow. J. Fluids Struct. 54, 361–389.

Please cite this article as: M.M. Rajamuni, M.C. Thompson and K. Hourigan, Vortex-induced vibration of elastically-mounted spheres: A comparison of the response of three degrees of freedom and one degree of freedom systems. Journal of Fluids and Structures (2019), https://doi.org/10.1016/j.jfluidstructs.2019.02.005.

Mi, L., Gottlieb, O., 2016. Nonlinear dynamics and internal resonances of a planar multi-tethered spherical aerostat in modulated flow. Meccanica 51, 2689–2712.
Mi, L., Gottlieb, O., 2017. Nonlinear dynamics and bifurcations of a spherical multi-tethered lighter-than-air system in uniform and modulated flow. Procedia Eng. 199, 717–722.
Mittal, R., 1999. Planar symmetry in the unsteady wake of a sphere. AIAA J. 37, TN 388–390.
Morsi, S.A., Alexander, A.J., 1972. An investigation of particle trajectories in two-phase flow systems. J. Fluid Mech. 55, 193–208. http://dx.doi.org/10.1017/S0022112072001806, URL:http://journals.cambridge.org/article_S0022112072001806.
Mougin, G., Magnaudet, J, 2001. Path instability of a rising bubble. Phys. Rev. Lett. 88, 014502.
Mougin, G., Magnaudet, J., 2006. Wake-induced forces and torques on a zigzagging/spiralling bubble. J. Fluid Mech. 567, 185–194.
Parkinson, G., 1989. Phenomena and modelling of flow-induced vibrations of bluff bodies. Prog. Aerosp. Sci. 26, 169–224.
Poon, E., Iaccarino, G., Ooi, A.S.H., Giacobello, M., 2009. Numerical studies of high Reynolds number flow past a stationary and rotating sphere. In: Proceedings of the 7th International Conference on CFD in the Minerals and Process Industries.
Poon, E.K.W., Ooi, A.S.H., Giacobello, M., Iaccarino, G., Chung, D., 2014. Flow past a transversely rotating sphere at Reynolds numbers above the laminar regime. J. Fluid Mech. 759, 751–781.
Pregnalato, C.J., 2003. Flow-Induced Vibrations of a Tethered Sphere (PhD), Monash University.
Rajamuni, M.M., Thompson, M.C., Hourigan, K., 2018a. Transverse flow-induced vibrations of a sphere. J. Fluid Mech. 837, 931–966.
Rajamuni, M.M., Thompson, M.C., Hourigan, K., 2018b. Vortex dynamics and vibration modes of a tethered sphere. J. Fluid Mech. (under review).
Rajamuni, M.M., Thompson, M.C., Hourigan, K., 2018c. Vortex-induced vibration of a transversely rotating sphere. J. Fluid Mech. 847, 786–820.
Roos, F.W., Willmarth, W.W., 1971. Some experimental results on sphere and disk drag. AIAA J. 9, 285–291.
Sarpkaya, T., 2004. A critical review of the intrinsic nature of vortex-induced vibrations. J. Fluids Struct. 19, 389–447.
Tomboulides, A.G., Orszag, S.A., 2000. Numerical investigation of transitional and weak turbulent flow past a sphere. J. Fluid Mech. 416, 45–73.
Williamson, C.H.K., Govardhan, R., 1997. Dynamics and forcing of a tethered sphere in a fluid flow. J. Fluids Struct. 11, 293–305.
Williamson, C.H.K., Govardhan, R., 2004. Vortex-induced vibrations. Annu. Rev. Fluid Mech. 36, 413–455.
Williamson, C.H.K., Govardhan, R., 2008. A brief review of recent results in vortex-induced vibrations. J. Wind Eng. Ind. Aerodyn. 96, 713–735.
Wu, X., Ge, F., Hong, Y., 2012. A review of recent studies on vortex-induced vibrations of long slender cylinders. J. Fluids Struct. 28, 292–308.

Please cite this article as: M.M. Rajamuni, M.C. Thompson and K. Hourigan, Vortex-induced vibration of elastically-mounted spheres: A comparison of the response of three degrees of freedom and one degree of freedom systems. Journal of Fluids and Structures (2019), https://doi.org/10.1016/j.jfluidstructs.2019.02.005.